



Melt infiltration for the preparation of finely dispersed Ni-FeO_x nanoparticles on SBA-15 for the hydrodeoxygenation of m-cresol

R. Deplazes^a, C.A. Teles^{b,*}, C. Ciotonea^{c,*}, A. Sfeir^a, N. Canilho^d, F. Richard^b, S. Royer^a

^a Université de Lille, CNRS, Centrale Lille, Université Artois, UMR 8181-UCCS-Unité de Catalyse et de Chimie du Solide, F-59000 Lille, France

^b Université de Poitiers, CNRS, Institut de Chimie des Milieux et Matériaux de Poitiers, UMR 7285, rue Michel Brunet, BP633, 86022 Poitiers, France

^c Université du Littoral Côte d'Opale, Unité de Chimie Environnementale et Interactions sur le Vivant-UCEIV, UR4492, SFR Condorcet FR CNRS 3417, 59140 Dunkerque, France

^d Laboratoire Lorrain de Chimie Moléculaire, L2CM UMR 7053 CNRS, Université de Lorraine, Vandœuvre-lès-Nancy, 54506 Nancy, France

ARTICLE INFO

Keywords:

M-cresol
Hydrodeoxygenation
Nickel-Iron bimetallic catalysts
SBA-15

ABSTRACT

The polymer-assisted melting infiltration method was used to finely disperse Ni, Fe and bimetallic Ni-Fe precursors in ordered mesoporous SBA-15 support. This approach allowed to obtain small Ni nanoparticles, in the order of 2 nm in size, with finely dispersed iron oxide surrounding metallic Ni, without evidence of Ni-Fe alloy formation. The catalysts were used in the HDO reaction of m-cresol at 300 °C and atmospheric pressure. The conversion of m-cresol was found to be dependent on Ni content, with the total reaction rate decreasing when Ni is partially replaced by iron. Toluene was the main product obtained for both, mono Ni and bimetallic Ni-Fe catalysts, thus suggesting that nickel nanoparticles when in the form of small sized particles, are the active sites for deoxygenation, independent on the presence of oxophilic iron site in their proximity. Such findings will serve for the further design of effective catalysts for the upgrading of lignin-derived bio-oil.

1. Introduction

Fossil hydrocarbons are at the basis of our modern society and economy, being always the main energy source or the raw material for more complex chemical products such as polymers, pharmaceutical substances and other specialty chemicals. Unfortunately, burning fossil fuels produce CO₂ and other problematic gases, and their exploitation also causes damages to the local environment in producing countries. Therefore, fossil hydrocarbons need to be replaced by renewable sources.

Lignocellulosic biomass can and does already serve as a source of chemical precursors for the production of fine chemicals and biofuels [1]. The lignin fraction could serve as source for aromatic compounds, even if it has proven to be more difficult to be exploited than cellulose and hemicelluloses [2]. In industry, lignin is a byproduct of the pulp mills and is in its vast majority burned to generate heat [3]. While this use eliminates waste and produces energy, it also leads to the loss of a valuable resource. Among the various methods for lignin processing, fast pyrolysis is probably the simplest one from a technical point of view. The process yields a pyrolysis oil, which is not suited for storage or for direct use in transport engines due to the high reactivity and corrosivity of the

oxygen containing compounds. Therefore, pyrolysis oils need to be treated and the oxygen removed, to fit the physicochemical standards required for fuel use. One process among others is the hydrodeoxygenation (HDO) process, during which oxygen is removed by reaction with hydrogen in the presence of a heterogeneous catalyst [4].

Different HDO catalytic systems have been reported to be active for the HDO reaction. Among them, the earliest were supported (Co,Ni)Mo-S sulphides whose main drawback is the lack of stability when employed on lignin compounds [5]. Noble metals such as Pt, Pd, Rh, are very active for the HDO of the phenolic compounds, but they usually yield saturated products which may not be completely deoxygenated [6–10]. In contrast, the use of oxophilic metals such as Ru, Fe as active phase or counterparts, or oxophilic supports such as ZrO₂, TiO₂ or Nb₂O₅ can promote direct deoxygenation to aromatic products [11–18]. As compared to noble metals, Ni is a highly abundant element in the earth's crust and is therefore readily available and cheap, which makes it an interesting alternative for industrial applications. However, due to its high hydrogenation activity, Ni catalysts usually promote the hydrogenation pathway during HDO, yielding ketones and alcohols as products [19,20]. This could potentially be changed by increasing the catalyst oxophilicity through the addition of a second metal with a superior

* Corresponding authors.

E-mail addresses: camila.abreu.teles@univ-poitiers.fr (C.A. Teles), carmen.ciotonea@eilco.univ-littoral.fr (C. Ciotonea).

<https://doi.org/10.1016/j.cattod.2024.114514>

Received 17 September 2023; Received in revised form 20 December 2023; Accepted 7 January 2024

Available online 11 January 2024

0920-5861/© 2024 The Author(s). Published by Elsevier B.V. This is an open access article under the CC BY-NC-ND license (<http://creativecommons.org/licenses/by-nc-nd/4.0/>).

oxophilicity. One cheap and abundant metal with superior oxophilicity is Fe [21]. It has been reported that the addition of Fe influences the selectivity of Ni catalyst and is able to inhibit the hydrogenation of aromatic rings, thus favoring the deoxygenation route [22,23]. Fang et al. for example, reported an increase in the conversion of guaiacol by tuning the Ni/Fe ratio [24]. Nie et al. found an enhancement in the HDO of *m*-cresol over NiFe/SiO₂ catalyst; Ni/SiO₂ producing methylcyclohexanone as major product while the introduction of Fe orientated the reaction toward the production of toluene [25]. Likewise, Han et al. found the same tendency in the HDO of phenol. But in this case, the conversion was dependent on the Ni/Fe ratio, showing that much Fe may have a negative effect on conversion [26]. Thus, doping of Ni with Fe can effectively combine the hydrogenating properties of Ni with the superior oxophilicity of Fe and it may be possible to change the catalyst selectivity towards the production of deoxygenated products, without complete hydrogenation of the aromatic ring. However, to the best of our knowledge, in all of the reported Ni-Fe catalytic systems, the catalysts always present large metallic particles. These, like in the case of Ni, favor hydrogenation but also hydrogenolysis routes. Smaller Ni nanoparticles have been recently reported to increase deoxygenation affording the production of aromatics with yields above 80%, but what about controlling particle size of Ni-Fe bimetallic catalysts?

In the present work, we propose a synthesis approach to prepare calibrated small Ni-Fe nanoparticles. Silica type SBA-15 was used as a support, owing to its several advantages such as hydrothermal stability, high surface area, controllable and adjustable mesoporosity, thus allowing the diffusion of large reactants. The presence of mesopore channels and secondary micropores permits the confinement and control of metal particles size, besides avoiding metal sintering. Then, a series of mono and bimetallic Ni-Fe supported on SBA-15-type silica catalysts was prepared and tested in the HDO of *m*-cresol at gas phase and atmospheric pressure. A set of characterization was performed in order to describe the materials properties and correlate properties with catalyst activity.

2. Experimental section

2.1. Materials

All chemicals required to prepare the mesoporous SBA-15, as well as, the NiO and Fe₂O₃ containing materials, were used as received: Si (OC₂H₅)₄ (TEOS, 98 wt%, Sigma-Aldrich), non-ionic triblock copolymer Pluronic P123 (poly(ethylene oxide)-block-poly(propylene oxide)-block-poly(ethylene oxide)-block, PEO₂₀PPO₇₀PEO₂₀, MW = 5800, Aldrich), hydrochloric acid (HCl, 37 wt%, CARLO ERBA Reagents), nickel nitrate (Ni(NO₃)₂·6 H₂O, 98%, Alfa Aesar), iron nitrate (Fe(NO₃)₃·9H₂O, 98%, Acros Organics).

2.2. Support preparation

SBA-15 was synthesized by a conventional synthesis procedure in acidic conditions. Deionised water (6.5 L), HCl (37%; 1 L) and Pluronic P123 (200 g) were firstly mixed in a 10 L glass reactor and stirred for 24 h at 40 °C. Then, the silicon source, TEOS (480 mL), was added dropwise and the solution stirred at 40 °C for 24 h. Then, the temperature was increased to 96 °C and kept for more 48 h. After cooling to room temperature, the precipitated was filtered, washed with deionized water and dried at 80 °C overnight.

2.3. Catalyst preparation

Ni-Fe supported on SBA-15 catalysts were prepared by a “polymer-assisted” Melt Infiltration (MI) method, as previously reported [27]. This method is based on the infiltration of molten precursors into the support porosity with the presence of the support polymer porogen. Herein, the non-calcined SBA-15 support (thus still containing the P123 polymer

porogen) and the nitrate precursors are ground together until obtain a homogeneous powder. Then, the powder is subjected to a thermal treatment at the metal's nitrate melting point temperature, in which the precursor melts into the pores of the support through capillary forces. In this work, appropriate amount of the precursors Ni(NO₃)₂·6H₂O and Fe(NO₃)₃·9H₂O were incorporated into the non-calcined SBA-15 by gentle grinding at ambient conditions for around 30 min. The resulting powders when containing Ni were then treated in a teflon autoclave at 57 °C (melting point of the Ni nitrate) and at 49 °C (melting point of the Fe nitrate) for Fe-containing materials, during 4 days. The materials were further calcined at 500 °C for 6 h (heating ramp of 1.5 °C min⁻¹). The materials were prepared by varying the content of Ni and Fe (Ni/Fe being 0/10, 2.5/7.5, 5/5, 7.5/2.5, 10/0) keeping the total content of Ni-Fe in 10 wt%.

2.4. Catalyst characterization

Ni and Fe loadings were determined by inductively coupled plasma optical emission spectroscopy (ICP-OES) on an Agilent 5110 Vertical Dual View ICP-OES equipped with a OneNeb nebulizer instrument. Before analysis, the samples were digested using concentrated nitric acid and hydrofluoric acid on a microwave heating system.

Textural properties were determined by N₂-physorption analysis at –196 °C on a Micromeritics Tristar III instrument. Before analysis, the samples were outgassed under dynamic vacuum at 350 °C for 3 h. Specific surface area was determined using the multipoint B.E.T. algorithm. Mesopore size distribution was determined using the B.J.H. equation applied to the desorption branch and pore volume was determined at $p/p_0 = 0.98$, on the adsorption branch. The micropore surface and microporous volume were determined by the t-plot method.

Powder X-ray diffraction (XRD) analysis was performed using a Bruker X-ray AXS D8 Advance X-ray diffractometer in Bragg-Brentano geometry configuration. XRD patterns in the wide-angle range were recorded with Cu K α radiation ($\lambda = 0.154$ nm) in the 10–80° 2 θ range with a step size of 0.05° each 2 s. Phase identification was made by comparison with the ICDD database. In order to follow the evolution of the phases, in-situ XRD analysis under H₂ flow was performed using the same equipment. In this case, the samples were analysed on a Pt sample holder with three reflections at 2 $\theta = 39.765^\circ$, 46.244° and 67.456°, which were not taken into consideration for the interpretation of the diffractograms. The analyses were performed by flowing 30 mL min⁻¹ of 3.0 vol% of H₂ in N₂, varying temperature from 30 °C up to 600 °C (10 °C min⁻¹). The diffractograms were recorded in the 2 θ range between 10–80° with a step size = 0.05° and step time = 2 s

Support morphology and metal dispersion state were analysed by transmission electron microscopy (TEM) on a TITAN Themis 3007 S/TEM equipped with a high brightness Schottky field emission gun, a probe aberration corrector, super-X detector system with four windowless silicon drift detectors for electron dispersive X-ray spectroscopy (EDX) and several annular dark field detectors. The experiments have been performed at 300 kV with semi-convergence angle of about 20 mrad, probe size of the order of 500 pm and probe current at around 100 pA. For high angle annular dark field (HAADF) imaging the camera length has been chosen so that the collection angles have been between 50 and 200 mrad. The EDX mapping has been obtained in multi-frame spectrum imaging mode with dwell time per pixel of about 15 μ s and continuously scanning frames until the total acquisition time of about 15 to 20 min. The samples were first reduced at 800 °C (5 °C min⁻¹) for 1 h and then embedded in a polymeric resin, sliced into 50 nm-thick sections using an ultramicrotome and deposited on a carbon grid for analysis.

The reducibility of the catalysts was studied by temperature-programmed reduction (H₂-TPR) on a Micromeritics Autochem II 2920 equipment. Before analysis, the solids were heated at 500 °C under 50 mL min⁻¹ of air flow (10 °C min⁻¹) during 1 h. After cooling down to room temperature, the temperature-programmed reduction was

performed up to 900 °C using a 50 mL min⁻¹ flow of 5.0 vol% H₂ in Ar, and a temperature ramp of 5 °C min⁻¹. The consumption of H₂ was quantified using a TCD.

The metal dispersion was determined by CO chemisorption analysis. The samples were firstly reduced at 600 °C (5 °C min⁻¹), under pure hydrogen flow (30 mL min⁻¹) during 1 h. The reactor was then cooled down to 30 °C under helium (30 mL min⁻¹) and successive pulses of pure CO (0.465 mL) were injected each 3 min. CO was quantified by a gas phase chromatograph equipped with a TCD detector and a Porapak Q column, allowing the quantification of CO uptake.

The surface composition of the calcined and reduced samples was evaluated by using X-ray photoelectron spectroscopy (XPS) analysis. The analyses were performed on a Kratos Analytical Axis Ultra DLD spectrometer, equipped with a monochromatic Al K α X-ray source (1486.6 eV) operating at 225 W (15 kV, 15 mA). The charge neutralizer system was used for all acquisitions done at a Pass Energy of 20 eV and a step size of 0.05 eV. Fresh samples were analyzed under ultra-high vacuum (UHV, 5.10⁻¹⁰ torr). The samples were reduced under 50 mL min⁻¹ of pure H₂ at 600 °C (5 °C min⁻¹, 1 h) in a high-temperature cell attached to the XPS instrument. Afterwards the samples were cooled under H₂, and then transferred under UHV to the XPS analysis chamber, without re-exposure to air. Binding energies (BE) were referenced to the unresolved Si 2p doublet for SBA-15 positioned at 103.5 eV. Simulation of the experimental signals was carried out with CasaXPS software using mixed Gaussian (70%)/Lorentzian (30%) peaks except for metallic nickel, where LA (1.1,2.2,10) line shape was used. Semiquantitative analysis was performed after the subtraction of Shirley type backgrounds.

2.5. HDO of *m*-cresol

The HDO reaction of *m*-cresol was carried out in a fixed-bed flow reactor system, operating at 300 °C under atmospheric pressure. A H₂/*m*-cresol molar ratio was fixed at 90. Before the reaction, the catalysts were reduced in situ under pure hydrogen (50 mL min⁻¹) at 600 °C (5 °C min⁻¹) for 1 h. The reactant feedstock, composed by *m*-cresol as the reactant (7 mol.%), decane as an internal standard (3 mol.%) and heptane as the solvent, was introduced at the top of the reactor by using a push-syringe. W/F values, defined as the ratio of catalyst weight (in g) and the molar flow rate of *m*-cresol (in mol h⁻¹) were varied in order to obtain comparable levels of conversion (around 10%). The line at the reactor outlet was maintained at 5 °C using a circulator Huber mini-chiller in order to condense any unconverted reactant and products. The first liquid sample was collected after 30 min of reaction and analysed by a Varian 430 chromatograph equipped with a DB-5 capillary column and a flame-ionization detector (FID). The conversion of *m*-cresol and product selectivity were calculated by using Eqs. (1) and (2):

$$X(\text{in}\%) = \frac{n_{m\text{-cresol}}^0 - n_{m\text{-cresol}}}{n_{m\text{-cresol}}^0} \times 100 \quad (1)$$

$$S_i(\text{in mol}\%) = \frac{n_i}{n_{m\text{-cresol}}^0 - n_{m\text{-cresol}}} \times 100 \quad (2)$$

Where $n_{m\text{-cresol}}^0$ and $n_{m\text{-cresol}}$ are the initial and after 30 min of reaction number of moles of *m*-cresol, respectively; n_i is the number of moles of a given *i* product.

Assuming a pseudo-first-order reaction rate, the total kinetic rate constant (k_{TOT} in mmol g_{Ni}⁻¹ h⁻¹) and the kinetic rate constants for the different reactions pathways were calculated using the Eqs. (3) and (4):

$$k_{\text{TOT}}(\text{in mmol g}_{\text{Ni}}^{-1} \text{ h}^{-1}) = \frac{-FLn(1-X)}{w \cdot (\% \text{Ni})} \quad (3)$$

$$k_y(\text{in mmol g}^{-1} \text{ h}^{-1}) = r_{\text{TOT}} \cdot S_y \quad (4)$$

Where k_{TOT} is the total kinetic rate constant determined for the global

transformation of *m*-cresol and k_y are the kinetic rate constants for the different reaction pathways, X is the *m*-cresol conversion, F is the *m*-cresol molar flow rate (in mmol h⁻¹), w is catalyst weight (in g), %Ni is the Ni content measured by ICP-OES and S_y is the selectivity to the different products: toluene for the deoxygenation route (DDO), 3-methylcyclohexanone, 3-methylcyclohexanol, methylcyclohexene isomers for the hydrogenation route (HYD), and phenol for the hydrogenolysis route (HYG).

3. Results

3.1. Catalyst characterization

Elemental analysis of the calcined samples is showed in Table 1. All samples presented contents of Ni and/or Fe close to the expected values, indicating the efficiency of the synthesis approach used to incorporated the selected metal content.

Wide-angle XRD analysis (showed in Fig. 1a) was used to obtain for phase identification on the calcined samples. For all samples no or very low intensity and broad peaks were detected besides the broad peak centered at 22°, which is characteristic of amorphous silica, thus indicating the formation of very finely dispersed nanoparticles on the support. In the diffractogram of the 10Ni/SBA sample, three main reflections positioned at 37°, 43° and 62° are observed in low intensity, which are associated to NiO crystalline phase (cubic structure, PDF 47-1049). With introduction of Fe, it is observed the appearance of peaks located at 33.1°, 35.6°, 49.4°, 54.0°, and 62.4°, characteristic of the Fe₂O₃ phase (cubic structure, PDF 01-080-7077). For the 10Fe/SBA sample however, no peaks were observed, indicating the formation of very small crystallites or the formation of an amorphous phase. These results show the good efficiency of the melt infiltration approach on the support containing porogen to produce very small metal particles, as previously reported [27,28].

In order to investigate the stability of such small particles, in situ reduction (30–600 °C) followed by XRD was performed (Fig. 1b and Fig. S1, ESI). For the 10Ni sample, the broad initial reflections characteristic of NiO phase disappears from 350 °C and a new reflection corresponding to Ni metallic phase (PDF 04-0850) is observed since 500 °C. This reflection still presents a broad shape even at 600 °C, which indicates the formation of small Ni(0) nanoparticles. For the 10Fe sample, reflections are never observed suggesting that iron phases remained too small on the support or amorphous. Regarding Ni-Fe

Table 1
Textural properties, reduction degree and average particle size of the NiFe-based materials.

Sample	Metal wt %		N ₂ physisorption				d _{Ni} ^f (nm)	D _{Ni} ^f (%)
	Ni ^a	Fe ^a	S _{BET} ^b (m ² g ⁻¹)	S _u ^c (m ² g ⁻¹)	V _p ^d (cm ³ g ⁻¹)	D _p ^e (nm)		
SBA-15	-	-	801	269	1.13	7.2	-	-
10Ni	8.9	-	721	115	1.16	7.2	2.6	26
7.5Ni2.5Fe	6.7	2.3	637	176	0.91	7.4	2.2 (2.5 h)	18
5Ni5Fe	4.2	4.3	689	211	0.98	7.2	2.1 (4.0 h)	5
10Fe	-	8.6	681	193	1.00	7.3	n.d.	-

^a Metal content determined by ICP-OES analysis;

^b S_{BET} specific surface calculated with BET equation;

^c S_u microporous surface with t-plot;

^d V_p pore volume at P/P₀ = 0.95;

^e D_p average pore diameter calculated with BJH on desorption method;

^f Average particle size calculated from TEM images of the reduced catalysts by using ImageJ software

^g Ni dispersion determined by CO chemisorption analysis.

^h Average particles size calculated from TEM images of calcined samples.

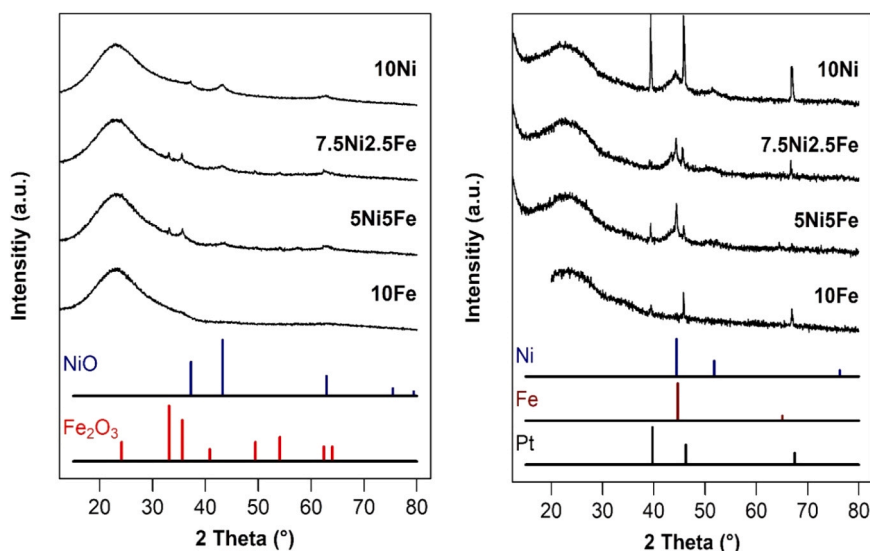


Fig. 1. XRD patterns for the (a) calcined and (b) Ni-Fe-based materials reduced in situ at 600 °C (all patterns are presented in Fig. S1, ESI). The reflections at 40, 46 and 48 ° are attributed to the Pt-based sample holder.

bimetallic samples, an additional reflection at around 44.5° starts to appear at 500 °C overlapping the broad one located at 44°, showing the presence of Ni particles with different size.

In order to evaluate the textural properties of the samples, nitrogen physisorption on the calcined samples was performed and the adsorption/desorption isotherms are presented in Fig. 2. The SBA-15 support presented a type IV(a) isotherm with hysteresis type H1, which are associated to mesoporous materials presenting a narrow distribution of cylindrical and tubular pores, good characteristics of SBA-15 material [29,30]. The parallel adsorption/desorption branches indicate a uniform arrangement of the pores. For the 10Fe sample, the same shape was obtained indicating no modification of the pores with the introduction of iron oxide. This agrees with the XRD profile which suggests the formation of very small particles well distributed on the support, thus not having any considerable influence on the support textural characteristics. For the Ni-containing samples, a latency in the closure of the desorption branch of the hysteresis can be observed, which can be associated to the presence of some small nickel oxide particles located inside the tubular pores, thus leading to constrictions [28].

The textural properties extracted from those isotherms are

summarized in Table 1. For all catalysts, a decrease in the surface area is observed after Ni and/or Fe infiltration (area of the bare SBA-15 decreasing from 801 m² g⁻¹ to between 627–721 m² g⁻¹). In addition, the microporous area significantly decreased by 22–57% as compared to the bare SBA-15 support, thus indicating that part of the metallic oxides is confined in the microporous intra-wall pores of the support. This has been previously reported for this kind of materials when prepared by melt infiltration method using the SBA-15 still containing the porogen [31]. On the contrary to the surface area, the pore volume (Table 1) and the pore size (Fig. 2b, Table 1) are not significantly affected by the deposition of the metal oxide phase.

HAADF-STEM images of calcined and reduced samples were collected to evaluate support architecture and location of the metal particles (Figs. 3, 4 and S2, ESI). The hexagonal honeycomb structure of the SBA-15 is well visible against the dark background in all HAADF images, indicating that the porous structure of the support remains unchanged after reduction at high temperature (800 °C in our case). For the Ni and Ni-Fe catalysts, in both calcined and reduced samples, the position and size of the nanoparticles indicate that the particles themselves are not just in the mesopores of the SBA-15, but mostly within

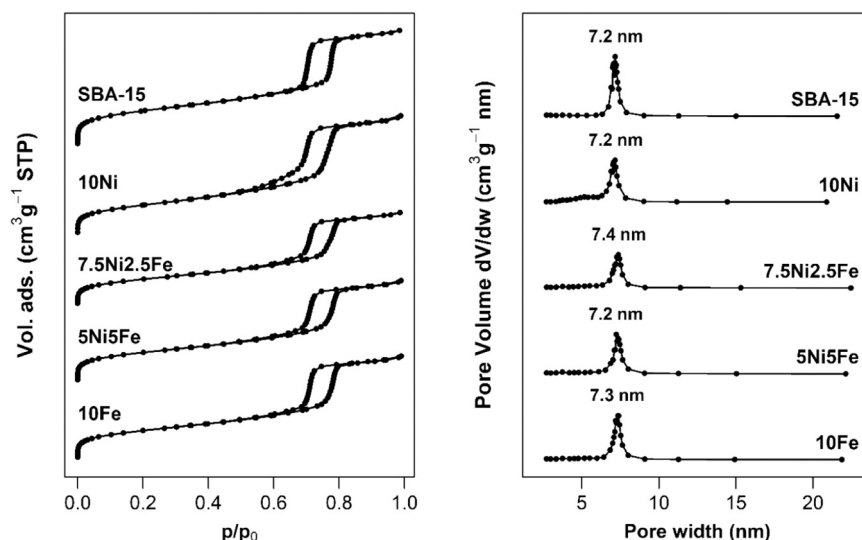


Fig. 2. (a) Adsorption/desorption nitrogen isotherms and (b) pore size distribution for the calcined materials.

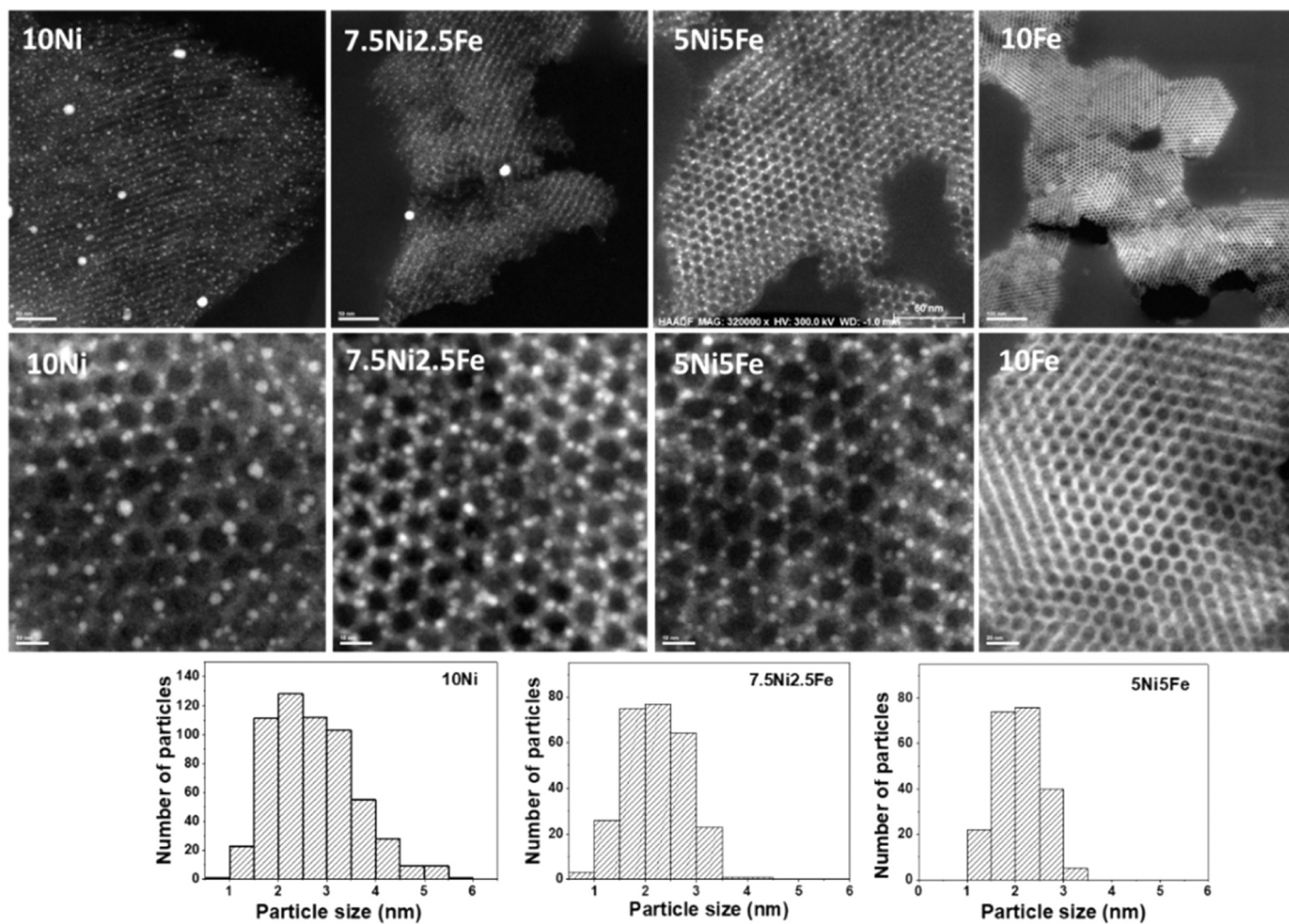


Fig. 3. Representative HAADF images and the respective histograms recovered onto multiple images for the Ni-Fe-based materials in the reduced form.

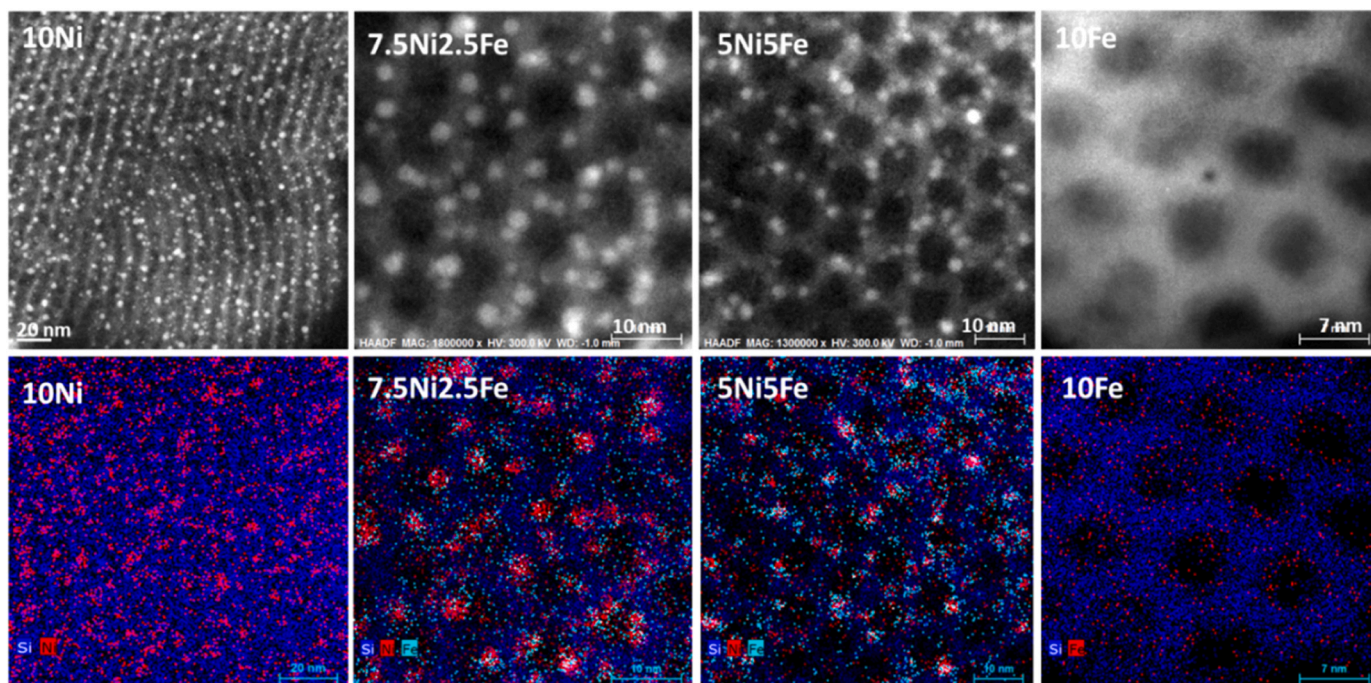


Fig. 4. Representative HAADF images and EDX elemental maps for the reduced NiFe catalysts.

their walls, i.e. within the microporous interconnection structure. The statistical analysis of the particle size, on the Ni-Fe calcined samples, shows average particles size of around 2.5 nm and 4 nm for 7.5Ni2.5Fe and 5Ni5Fe respectively. After reduction, the three catalysts lead to > 80% of particles of size < 4 nm for 10Ni, and < 3 nm of Ni-Fe catalysts, thus showing that there is not sintering after reduction at high temperatures. Average particle size (Table 1) is for the three catalysts in the 2.1–2.6 nm size. It should be noted, in some regions, external particles can be detected for Ni containing samples. When not located inside the support porosity, the particles are suggested to significant sintering during reduction, influencing the XRD patterns and explaining the appearance of narrow peaks overlapping the broad one. Only the 10Fe catalyst show no distinct particles, suggesting either that the Fe particles are close to a single atom distribution, or that a very heterogeneous distribution of Fe in the material is obtained (and leading to a lack in the area observed). The EDX elemental maps of the Ni containing materials (Fig. 5) clearly show Ni nanoparticles located in the pore walls and iron very finely dispersed onto the support and in proximity to the Ni nanoparticles. For 10Fe, EDX elemental maps confirm the presence of iron on the analyzed zones, even if no particles are visible. This result lets us to suppose that iron phase homogeneously incorporated the silica support.

Catalyst reducibility was evaluated by H₂-TPR analysis (Fig. 5). The reduction profile of 10Ni sample shows one main peak at 552 °C associated to the reduction of Ni(II) to Ni(0). This higher temperature is associated to the reduction of small NiO nanoparticles confined in the microporosity of the support, thus hardly accessible to reduction [27]. Additionally, there is a small peak at around 350 °C, likely to a small population of larger Ni particles probably located at the external surface of the SBA-15 (visible in rare cases, as in Fig. 3). For the 10Fe sample, two distinct peaks are observed at 406 °C and 828 °C, associated with the reduction of iron oxide in two steps: Fe(III) to Fe(II) and the beginning of some Fe(II) reduction to Fe(0), respectively. Herein, the temperatures are higher compared to those found in the literature for the reduction of iron oxide which is probably associated to the divided state of the iron phase, and its localization inside the porosity of the support. Replacing 2.5% Ni with Fe (7.5Ni2.5Fe sample) it is possible to observe the first peak (371 °C), associated with the reduction of Fe(III), and the second peak, associated the reduction of Ni(II), slightly shifting to lower temperatures (from 550 to 504 °C). A very similar profile is observed for the 5Ni5Fe sample. However, the first peak associated to the reduction of Fe(III) is now at 416 °C. For both Ni-Fe samples, the peak at high temperature (> 800 °C) related to the reduction of Fe(II) is not further observed. This suggests that the dissociation of H₂ by Ni may accelerates

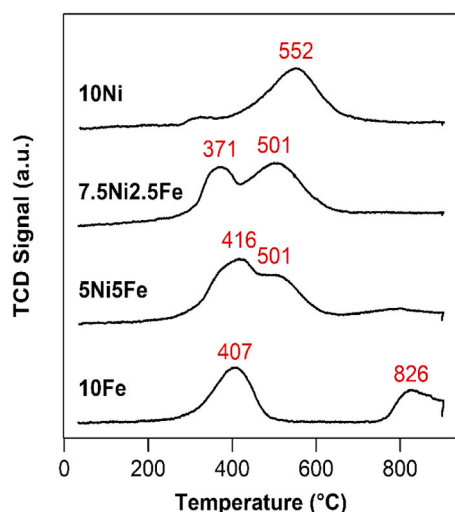


Fig. 5. TPR profiles for containing he Ni-Fe-based materials.

the reduction of iron oxide, illustrating the interaction between Ni and Fe [26]. For all Ni-containing samples, the degree of Ni reduction was close to 100%, while for 10Fe sample, only 76% of reduction of Fe(III) into Fe(II) at 900 °C was obtained.

The surface chemical composition of the calcined samples and after reduction (600 °C, flow of pure H₂, 1 h), was determined by XPS analysis (Fig. 6 and S4, ESI). In the Ni 2p region, the high-resolution spectra for all calcined samples containing Ni (10Ni, 7.5Ni2.5Fe and 5Ni5Fe, Fig. S2), show a well resolved Ni(OH)₂ doublet with its corresponding satellite peak at BE of ~ 856.5 eV for Ni(II) 2p_{3/2}, ~ 874.2 eV for Ni(II) 2p_{1/2}, along with a satellite peak around 862.4 eV, which is in agreement with the literature [32,33]. Upon reduction (Fig. 6), all peaks shift to lower binding energy thus indicating successful reduction of Ni(II) to Ni(0). The quantification of nickel species after in situ reduction is presented in Table 2. For 10Ni sample, 75% of the surface Ni species were reduced into Ni(0), with the remaining as NiO. Comparable or slightly higher reduction degree was observed for the bimetallic catalysts, with 78% and 89% of reduction for 7.5Ni2.5Fe and 5Ni5Fe, respectively.

Looking at the Fe 2p region for the 10Fe reduced sample (Fig. S2, ESI), it is clearly observed the reduction of Fe(III) present on the calcined sample, to Fe(II), with the corresponding peaks at BE of ~ 711.5 eV, ~ 725 eV for Fe(III) 2p_{3/2} and Fe(III) 2p_{1/2}, respectively, and at BE of ~ 710.8 eV, ~ 724.3 eV, and ~ 716 eV for Fe(II) 2p_{3/2} and Fe(II) 2p_{1/2} and the satellite, respectively. In the case of the 7.5Ni2.5Fe sample, no peaks characteristic of iron was detected, indicating a to low concentration of iron to be detected by XPS even if evidenced by TEM. Besides that, the higher concentration of nickel leads to more intense Auger peaks in the region (Ni LMM), thus making accurate analysis difficult. In this case, taking into consideration the intensity of the Auger peak for the 5Ni5Fe sample in the Fe2p region, only Fe(II) species is identified. The results indicate that under these reduction conditions, iron could not be reduced to the metallic form, thus suggesting that the Ni-Fe samples are represented by Ni nanoparticles confined in the micropores and FeO finely dispersed on the silica, in proximity with Ni particles as observed in the TEM images. Before the catalytic test, the reduction step allows to obtain mainly Ni particles under metallic phase whereas iron was only reduced into Fe(II) species. Therefore, in bimetallic samples we can assume that the active phase is composed by finely dispersed iron oxide surrounding small reduced Ni nanoparticles.

3.2. HDO reaction of *m*-cresol

The product distribution obtained at same level of *m*-cresol conversion (around 10%) for all of catalysts containing Ni is presented in Table 3. 10Fe catalyst did not show measurable conversion in the conditions used here, which may be due to the absence of metallic iron phase, as demonstrated by XPS results in which iron is present as Fe(II) after reduction at 600 °C. The catalyst was also tested after reduction at 800 °C, with only traces of toluene and xylene being obtained (*m*-cresol conversion < 2%). For the Ni-based catalysts, toluene was the main product obtained, with selectivity almost constant (65–73%). Other products obtained are 3-methylcyclohexanone, 3-methylcyclohexanol, phenol and traces of methylcyclohexenes, besides xylene.

Product distribution obtained here agrees very well with reaction mechanism proposed in the literature for the transformation of *m*-cresol at similar reaction conditions (Scheme 1). The reaction can proceed via three main parallel routes, depending on the type of catalyst: (i) direct deoxygenation (DDO) to produce toluene, in which the C-O bond is directly cleaved or may involves the formation of the tautomer intermediate. In this case, the carbonyl bond of the tautomer is selectively hydrogenated producing an unsaturated alcohol which is rapidly converted to toluene; (ii) hydrogenation (HYD) of the tautomer aromatic ring producing 3-methylcyclohexanone and further 3-methylcyclohexanol, the last one may be dehydrated to methylcyclohexenes if catalyst contain acid sites; and (iii) hydrogenolysis (HYG) of the methyl group

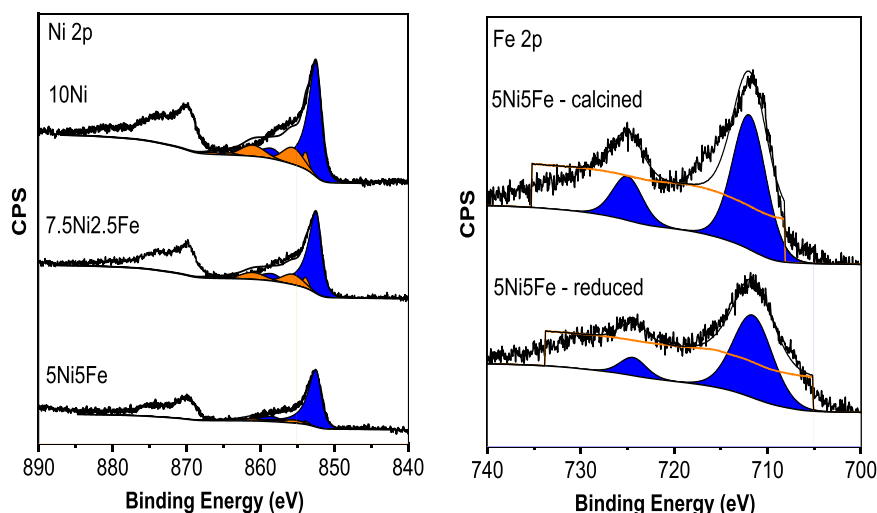


Fig. 6. Ni 2p and Fe 2p core level for the Ni-Fe catalysts reduced at 600 °C.

Table 2

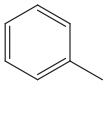
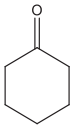
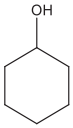
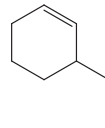
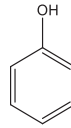
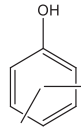
Percentage of Ni and Fe species obtained from the curve-fitted values of XP spectra of the Ni-Fe-based catalysts after in situ reduction under pure hydrogen at 600 °C, 1 h.

Catalyst	Atomic composition (%)						% at surface	
	Ni (II)	Ni (0)	Fe (III)	Fe (II)	Fe (0)	Si	Ni	Fe
10Ni	25	75	-	-	-	95	5	-
7.5Ni2.5Fe	22	78	n.d.	n.d.	n.d.	96.4	3.7	-
5Ni5Fe	11	89	-	100	-	95.4	2.4	1.6
10Fe	-	-	-	100	-	89.5	-	10.5

producing phenol and methane [10,17,34–36]. Other reaction pathways may be also present depending on catalyst acidity, such as disproportionation (DISP) leading to the formation of phenol and xylenols [25,37,38]. The orientation of the conversion to each reaction pathway strongly depends on the nature of the metallic phase and support. For instance, at temperature of around 300 °C and atmospheric pressure, hydrogenating metals such as Pt, Pd, Rh and Ni favor the hydrogenation route producing ketone and alcohol as major products, with Ni also promotes hydrogenolysis [6,9,39]. More oxophilic metals such as Ru and Fe promote the direct cleavage of m-cresol yielding toluene [10,14,40,41]. The nature of support plays an important role and may modify the activity of those metals. For example, over acidic supports such as alumina or zeolites, metals such as Pd, Pt, Ni will promote the alcohol dehydration to

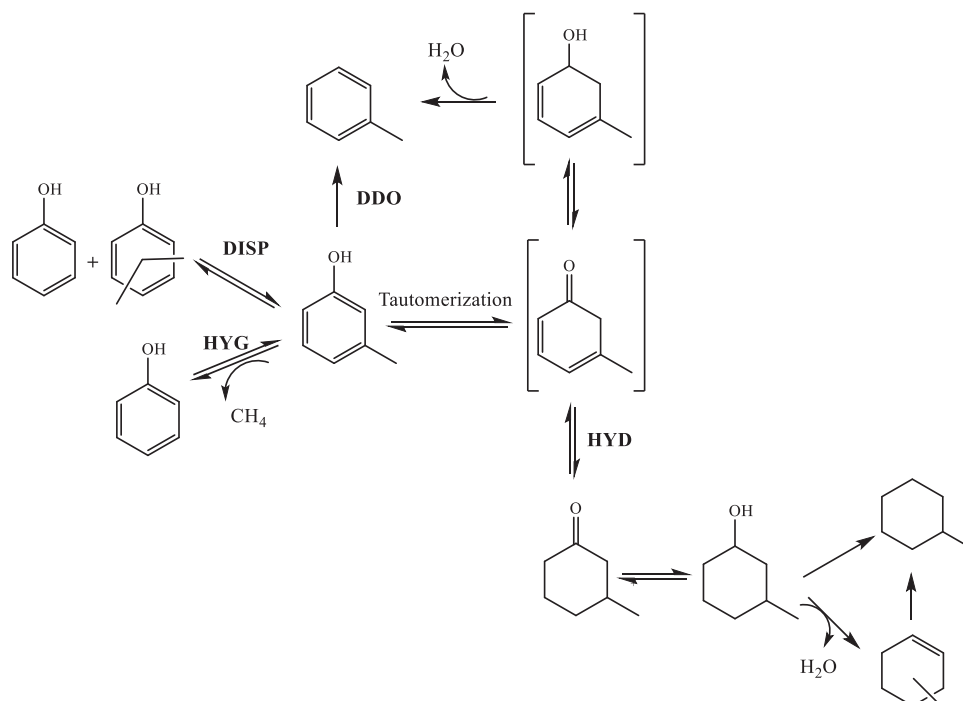
Table 3

Product distribution obtained in the transformation of m-cresol over the NiFe-based catalysts ($T_{\text{reduction}} = 600 \text{ °C}$, $T_{\text{reaction}} = 300 \text{ °C}$, 1 atm, 30 min of TOS).

Catalyst	W/F (g h mol ⁻¹)	Conversion (%)	Selectivity (%)						Ref
									
10Ni	6	10	73	14	2	1	6	2	This work
7.5Ni2.5Fe	13	18	67	18	4	1	4	3	
5Ni5Fe	124	10	65	5	1	7	13	9	
10Ni+ 10Fe ^a	8	12	68	17	2	2	8	4	[25]
5Ni/SiO ₂	50	16	14	33	11	-	-	28 ^b	
5Ni5Fe/SiO ₂	50	14	53	-	-	-	-	45 ^b	
5Fe/SiO ₂	50	9	60	-	-	-	-	40 ^b	

a: Physical mixture of equivalent content of 10Ni and 10Fe catalysts.

b: selectivity into disproportionation products (phenol and xylenols)



Scheme 1. Reaction pathways proposed for the HDO of m-cresol over Ni-based catalysts.

(varying between 2–22 nm) in the HDO of m-cresol (300 °C, 1 atm) and showed that decreasing Ni particle size improves the intrinsic reaction rate of HDO by 24 times. By using DFT calculations, the authors simulated the different sites (terrace-Ni(111); edge-Ni(211) and corner-defected Ni(211)) and the adsorption mode and deoxygenation of phenol. The adsorption energy of phenol, activation and reaction energy significantly varied depending on the type of site, decreasing in the following order: terrace > edge > corner, thus confirming that edge and corner type sites interact strongly with the oxygenated compound thus favoring the deoxygenation pathway. Therefore, this explains the high selectivity to toluene (73%) observed for our 10Ni catalyst, which also presents small Ni nanoparticles (average size of 2.6 nm, Table 1).

By introducing Fe in the catalyst composition, not much difference is observed in the selectivity to toluene, already significant for 10Ni, and the product distribution for the 7.5Ni2.5Fe catalyst remains almost comparable, with a slight increase in the selectivity to 3-methylcyclohexanone and decrease in the selectivity to phenol (6 to 4%). Increasing the content of iron (5Ni5Fe), the selectivity to 3-methylcyclohexanone decreases (from 14 to 5%), while yields of products from disproportionation route (phenol and xylenol) increases. DISP route is promoted by the non-reduced iron oxide, in this case Fe(II) species as detected by XPS analysis, a result in accordance with literature about iron supported catalysts in the HDO of m-cresol [25]. A physical mixture of 10Ni and 10Fe catalysts was also tested in order to verify the effect of iron in catalyst composition is associated to the Fe proximity with Ni. Same product distribution and conversion in equivalent W/F value compared to 10Ni catalyst was obtained, thus indicating that Ni particles are the effective active sites for m-cresol conversion and that Fe(II) species, when isolated from Ni(0), are almost inactive under the conditions at which Ni(0) works.

To better understand the role of Ni nanoparticles, the total reaction rate as well as the rates calculated for each reaction pathway are listed in Table 4. The total reaction rate strongly decreases replacing Ni by Fe, clearly indicating that Ni nanoparticles are the active species responsible for the reaction, while iron seems to have a minor role in orientating the reaction towards deoxygenation. However, assuming that the reaction happens only over the Ni nanoparticles, the DDO rate experimentally obtained for the 5Ni5Fe catalyst is much lower compared to the

Table 4

Reaction rate constant (in $\text{mmol g}_{\text{Ni}}^{-1} \text{h}^{-1}$) values calculated for the transformation of m-cresol and for each reaction pathway over NiFe-based catalysts (300 °C, atmospheric pressure).

Catalyst	k_{TOT}	k_{DDO}	k_{HYD}	k_{HYG}	k_{DISP}
10Ni	236.4	172.5	40.2	9.5	14.2
7.5Ni2.5Fe	180.5	120.9	41.5	1.8	16.2
5Ni5Fe	16.3	10.6	2.1	0.8	2.8

expected one calculated considering the activity of the 10Ni sample presented in Fig. 7. One hypothesis to explain that, would be that with a high Fe/Ni ratio, iron oxide partially covers Ni, thus reducing the exposed Ni surface for reaction with the consequence reduction of catalyst activity. In order to get evidences on this assumption, CO chemisorption was performed to measure the dispersion of Ni and results are reported in Table 1. The introduction of iron led to a decrease of

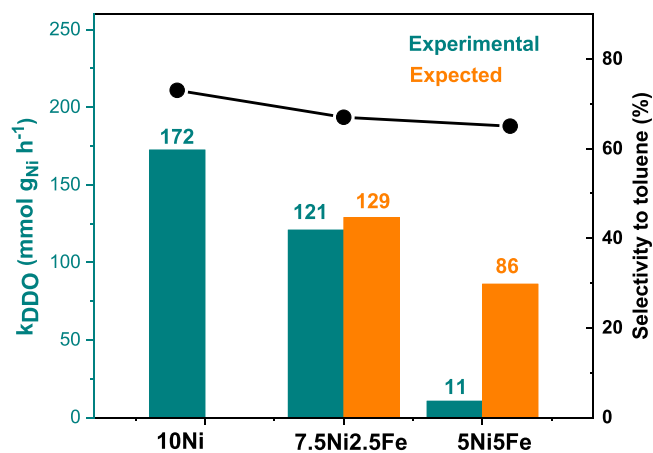


Fig. 7. Deoxygenation activity measured by k_{DDO} values (left axis) and selectivity measured by the percentage of toluene formed (right axis) of the Ni-Fe catalysts.

the dispersion values: 10Ni (26%) > 7.5Ni2.5Fe (18%) > 5Ni5Fe (5%). Based on these values, an increase of the metallic particle size is hence expected. Nevertheless, the TEM images showed the same particle size whatever the catalyst, thus evidencing that a part of Ni particles may be covered by FeO_x species and hence not accessible to reactants.

Ni-Fe based catalysts has been currently reported in the HDO reaction of phenolic compounds [13,25,26,48,49]. For example, Nie et al. investigated a series of Ni-Fe supported on commercial HiSil silica on the HDO of m-cresol using similar reaction conditions, i.e. 300 °C and atmospheric pressure [25]. Over the monometallic Ni catalyst, the dominant products were 3-methylcyclohexanone and 3-methylcyclohexanol (33.3% and 11.1% of selectivity, respectively) besides formation of DISP products such as xlenols and phenol (28% of selectivity). On Fe and Ni-Fe bimetallic catalysts, the hydrogenated products were negligible and toluene was the major product (varying between 52.6 to 60.2% in selectivity) besides DISP products (24.2 to 45.3%), likely observed in this work. To explain the results, the authors calculated the adsorption energy of m-cresol on Ni(111), Fe(110) and NiFe(111) alloy surface and showed that m-cresol preferentially adopts a flat adsorption configuration on both Ni(111) and NiFe(111) surfaces, but a slanted configuration on NiFe alloy. As a consequence, the interaction with oxygen atom of m-cresol is strongest on Fe followed by Ni-Fe alloy and negligible on Ni surface. However, unlike our work, they obtained a remarkable difference in product selectivity by introducing Fe in the Ni catalyst (toluene selectivity increasing from 14% on 5Ni/SiO₂ to 53% on 5Ni5Fe/SiO₂ catalyst), while maintaining comparable activity (conversion of 16 to 14% at same W/F value close to 50 g h mol⁻¹), as shown in Table 3. This may be from the fact of nickel content was kept constant (5 wt%) in the catalysts and the particles size of the metals was significantly larger (around 10 nm) compared to our materials (around 2 nm). As previously discussed, larger Ni nanoparticles size promotes HYD and HYG routes while smaller ones promote DDO route yielding toluene. Then, this explain the higher selectivity to HYD products on 5Ni/SiO₂ and the increase in deoxygenation when introducing Fe. It should be noted that the catalyst containing only Ni in our work was about 5 times more active than the one reported in that work,²⁵ which can be attributed to smaller particle size of Ni. In another work, Han et al. tested a series of Ni-Fe supported on mesoporous carbon spheres (MCSs) in the HDO of phenol [26]. In that case, the authors varied the Ni/Fe ratio and the reaction was performed in liquid phase at 250 °C and 5 MPa of total pressure. In these conditions, the reaction usually starts by ring hydrogenation producing cyclohexanol, which can be directly deoxygenated to cyclohexane via HYG of C-O bond, or produce cyclohexene via dehydration on acid catalysts, followed by hydrogenation to cyclohexane. In that case, all of catalysts were very active, reaching conversion in the order of 80–99% except 10Fe/MCSs which shows only 6.4% conversion. However, product selectivity varied as a function of catalyst composition. 10Ni/MCSs catalyst produced cyclohexanol as major product (88.2% in selectivity) and poor selectivity for the deoxygenated product cyclohexane (8.7%). By introducing iron and keeping the Ni/Fe molar ratio greater than 1, the conversion of phenol is still higher and the selectivity to cyclohexane continuously increases (up to 35%). With further increase in iron content, the selectivity is maintained but the conversion of phenol decreases, as observed in our present work. In this case, the authors also reported the formation of Ni-Fe alloy with particles size varying from 2.5 to 4.8 nm. It is important to note that, the catalyst which presented smaller particle size (2.5 nm) was the one with higher content of iron, and thus, less active.

Therefore, the results obtained in this work and abroad, indicate that Fe, as an oxophilic metal, can be used to promote the selective activation of m-cresol, inducing the cleavage of C-O bond. However, the catalyst activity is strong dependent on the Ni active sites for bonds hydrogenation and hydrogenolysis. Replacing Ni by Fe inhibit the H₂ chemisorption and dissociation on Ni surface thus decreasing the reaction rate. Our results further demonstrate that there is two ways to improve deoxygenation activity of Ni-based catalysts: (i) by alloying Ni with

appropriate amounts of an oxophilic metal such as Fe, or (ii) by decreasing Ni nanoparticle size. In that last case, small Ni nanoparticles play both roles, dissociation of hydrogen and activation of the C-O bond. Then, pure nickel catalyst, if stable small particles are obtained (<2–3 nm) can present selectivities to DDO products close to which obtained for Fe-modified larger Ni particles. To conclude, a careful control of particle size can be an efficient approach to maximize catalyst efficiency and orientate selectivity without any additive added to the main active element.

4. Conclusions

The present work investigated the reactivity of a series of mono and bimetallic Ni-Fe nanoparticles supported on SBA-15 in the HDO reaction of m-cresol at gas phase and atmospheric pressure. Melt infiltration synthesis was proposed to obtain very small and well dispersed Ni-Fe nanoparticles: Ni nanoparticles of around 2–2.5 nm confined in the secondary (low size) porosity of the walls of the mesoporous SBA-15 support. Iron is identified very finely dispersed onto the support, and in proximity to the Ni nanoparticles. Regarding catalyst reactivity, no significant difference was observed in the product distribution, with all catalysts presenting a high selectivity to the deoxygenated product, toluene (65–73%). However, the reaction rate is observed to significantly decrease when replacing Ni by Fe. These findings demonstrate that small Ni nanoparticles (2–2.5 nm) present active sites for deoxygenation of m-cresol through the direct deoxygenation pathway, with no advantage in introducing oxophilic counterparts to maximize aromatic production.

CRediT authorship contribution statement

Royer S.: Conceptualization, Funding acquisition, Project administration, Supervision, Validation, Visualization, Writing – review & editing. **Canilho N.:** Conceptualization, Funding acquisition, Supervision, Validation, Writing – review & editing. **Richard F.:** Conceptualization, Funding acquisition, Supervision, Validation, Visualization, Writing – review & editing. **Ciotonea C.:** Conceptualization, Data curation, Formal analysis, Methodology, Visualization, Writing – review & editing. **Sfeir A.:** Data curation, Formal analysis, Software, Writing – original draft. **Teles Camila Abreu:** Conceptualization, Data curation, Investigation, Methodology, Validation, Visualization, Writing – original draft, Writing – review & editing, Supervision. **Deplazes R.:** Data curation, Formal analysis, Investigation, Methodology, Writing – original draft.

Declaration of Competing Interest

The authors declare that they have no known competing financial interests or personal relationships that could have appeared to influence the work reported in this paper.

Data availability

Data will be made available on request.

Acknowledgements

This work was performed in the frame of the PYRODEOX project granted by the ANR (ANR-21-CE43-0006). C.A. Teles and F. Richard acknowledge financial support from the European Union (ERDF) and “Region Nouvelle Aquitaine”. The authors would like to thank Pardis Simon for XPS data acquisition and Anne-Sophie Mamede for data treatment, Laurence Burylo for XRD facility, and Maya Marinova for TEM images. The Chevreul Institute is thanked for its help in the development of this work through the ARCHI-CM project supported by the “Ministère de l’Enseignement Supérieur de la Recherche et de

l'Innovation", the region "Hauts-de-France", the ERDF program of the European Union and the "Métropole Européenne de Lille.

Appendix A. Supporting information

Supplementary data associated with this article can be found in the online version at doi:10.1016/j.cattod.2024.114514.

References

- [1] P. Gallezot, Conversion of biomass to selected chemical products, *Chem. Soc. Rev.* 41 (2012) 1538–1558, <https://doi.org/10.1039/C1CS15147A>.
- [2] A. Vishtal, A. Kraslawski, Challenges in industrial applications of technical lignin, *BioRes* 6 (3) (2011) 3547–3568.
- [3] A. Eraghi Kazzaz, P. Fatehi, Technical lignin and its potential modification routes: a mini-review, *Ind. Crops Prod.* 154 (2020) 112732, <https://doi.org/10.1016/j.indcrop.2020.112732>.
- [4] E. Furimsky, Catalytic hydrodeoxygenation, *Appl. Catal. A: Gen.* 199 (2000) 147–190, [https://doi.org/10.1016/S0926-860X\(99\)00555-4](https://doi.org/10.1016/S0926-860X(99)00555-4).
- [5] M. Edelman, Vapor-phase catalytic hydrodeoxygenation of benzofuran, *J. Catal.* 111 (1988) 243–253, [https://doi.org/10.1016/0021-9517\(88\)90083-8](https://doi.org/10.1016/0021-9517(88)90083-8).
- [6] C.A. Teles, R.C. Rabelo-Neto, J.R. de Lima, L.V. Mattos, D.E. Resasco, F.B. Noronha, The effect of metal type on hydrodeoxygenation of phenol over silica supported catalysts, *Catal. Lett.* 146 (2016) 1848–1857, <https://doi.org/10.1007/s10562-016-1815-5>.
- [7] C.A. Teles, R.C. Rabelo-Neto, G. Jacobs, B.H. Davis, D.E. Resasco, F.B. Noronha, Hydrodeoxygenation of phenol over zirconia-supported catalysts: the effect of metal type on reaction mechanism and catalyst deactivation, *ChemCatChem* 9 (2017) 2850–2863, <https://doi.org/10.1002/cctc.201700047>.
- [8] A. Gutierrez, R.K. Kaila, M.L. Honkela, R. Slioor, A.O.I. Krause, Hydrodeoxygenation of guaiacol on noble metal catalysts, *Catal. Today* 147 (2009) 239–246, <https://doi.org/10.1016/j.cattod.2008.10.037>.
- [9] C. Chen, G. Chen, F. Yang, H. Wang, J. Han, Q. Ge, X. Zhu, Vapor phase hydrodeoxygenation and hydrogenation of m-cresol on silica supported Ni, Pd and Pt catalysts, *Chem. Eng. Sci.* 135 (2015) 145–154, <https://doi.org/10.1016/j.ces.2015.04.054>.
- [10] Q. Tan, G. Wang, L. Nie, A. Dinse, C. Buda, J. Shabaker, D.E. Resasco, Different product distributions and mechanistic aspects of the hydrodeoxygenation of m-Cresol over platinum and ruthenium catalysts, *ACS Catal.* 5 (2015) 6271–6283, <https://doi.org/10.1021/acscatal.5b00765>.
- [11] Q. Tan, G. Wang, A. Long, A. Dinse, C. Buda, J. Shabaker, D.E. Resasco, Mechanistic analysis of the role of metal oxophilicity in the hydrodeoxygenation of anisole, *J. Catal.* 347 (2017) 102–115, <https://doi.org/10.1016/j.jcat.2017.01.008>.
- [12] T.N. Phan, C.H. Ko, Synergistic effects of Ru and Fe on titania-supported catalyst for enhanced anisole hydrodeoxygenation selectivity, *Catal. Today* 303 (2018) 219–226, <https://doi.org/10.1016/j.cattod.2017.08.025>.
- [13] P.-J. Hsu, J.-W. Jiang, Y.-C. Lin, Does a strong oxophilic promoter enhance direct deoxygenation? A Study of NiFe, NiMo, and NiW Catalysts in p-Cresol Conversion, *ACS Sustain. Chem. Eng.* 6 (2018) 660–667, <https://doi.org/10.1021/acsschemeng.7b03010>.
- [14] A. Kumar, A. Kumar, B. Biswas, J. Kumar, S.R. Yenumala, T. Bhaskar, Hydrodeoxygenation of m-Cresol over Ru based catalysts: influence of catalyst support on m-Cresol conversion and methylcyclohexane selectivity, *Renew. Energy* 151 (2020) 687–697.
- [15] Y. Hong, H. Zhang, J. Sun, K.M. Ayman, A.J.R. Hensley, M. Gu, M.H. Engelhard, J.-S. McEwen, Y. Wang, Synergistic catalysis between Pd and Fe in gas phase hydrodeoxygenation of m-Cresol, *ACS Catal.* 4 (2014) 3335–3345, <https://doi.org/10.1021/cs500578g>.
- [16] P.M. de Souza, R.C. Rabelo-Neto, L.E.P. Borges, G. Jacobs, B.H. Davis, D.E. Resasco, F.B. Noronha, Hydrodeoxygenation of phenol over Pd Catalysts. Effect of support on reaction mechanism and catalyst deactivation, *ACS Catal.* 7 (2017) 2058–2073, <https://doi.org/10.1021/acscatal.6b02022>.
- [17] C.A. Teles, P.M. de Souza, R.C. Rabelo-Neto, M.B. Griffin, C. Mukarakate, K.A. Orton, D.E. Resasco, F.B. Noronha, Catalytic upgrading of biomass pyrolysis vapors and model compounds using niobia supported Pd catalyst, *Appl. Catal. B: Environ.* 238 (2018) 38–50, <https://doi.org/10.1016/j.apcatb.2018.06.073>.
- [18] C.A. Teles, P.M. de Souza, R.C. Rabelo-Neto, N. Duong, J. Quiroz, P.H. Camargo, G. Jacobs, D.E. Resasco, F.B. Noronha, Role of the metal-support interface in the hydrodeoxygenation reaction of phenol, *Catal. Appl. B* 277 (2020) 119238, <https://doi.org/10.1016/j.apcatb.2020.119238>.
- [19] M. Lu, Y. Jiang, P. Zhang, J. Zhu, M. Li, Y. Shan, J. Shen, C. Song, Hydrodeoxygenation of guaiacol catalyzed by ZrO₂-CeO₂-supported nickel catalysts with high loading, *Energy Fuels* 34 (2020) 4685–4692, <https://doi.org/10.1021/acs.energyfuels.0c00445>.
- [20] S. Jin, Z. Xiao, C. Li, X. Chen, L. Wang, J. Xing, W. Li, C. Liang, Catalytic hydrodeoxygenation of anisole as lignin model compound over supported nickel catalysts, *Catal. Today* 234 (2014) 125–132, <https://doi.org/10.1016/j.cattod.2014.02.014>.
- [21] K.P. Kepp, A quantitative scale of oxophilicity and thiophilicity, *Inorg. Chem.* 55 (2016) 9461–9470, <https://doi.org/10.1021/acs.inorgchem.6b01702>.
- [22] D. Shi, A. Sadier, J.-S. Girardon, A.-S. Mamede, C. Ciotonea, M. Marinova, L. Stievano, M.T. Sougrati, C. La Fontaine, S. Paul, R. Wojcieszak, E. Marceau, Probing the core and surface composition of nanoalloy to rationalize its selectivity: study of Ni-Fe/SiO₂ catalysts for liquid-phase hydrogenation, *Chem. Catal.* 2 (2022) 1686–1708, <https://doi.org/10.1016/j.cheecat.2022.04.009>.
- [23] D. Shi, R. Wojcieszak, S. Paul, E. Marceau, Ni promotion by Fe: what benefits for catalytic hydrogenation, *Catalysts* 9 (2019) 451, <https://doi.org/10.3390/catal9050451>.
- [24] H. Fang, J. Zheng, X. Luo, J. Du, A. Roldan, S. Leoni, Y. Yuan, Product tunable behavior of carbon nanotubes-supported Ni-Fe catalysts for guaiacol hydrodeoxygenation, *Appl. Catal. A: Gen.* 529 (2017) 20–31, <https://doi.org/10.1016/j.apcata.2016.10.011>.
- [25] L. Nie, P.M. de Souza, F.B. Noronha, W. An, T. Sooknoi, D.E. Resasco, Selective conversion of m-cresol to toluene over bimetallic Ni-Fe catalysts, *J. Mol. Catal. A: Chem.* 388–389 (2014) 47–55, <https://doi.org/10.1016/j.molcata.2013.09.029>.
- [26] Q. Han, M.U. Rehman, J. Wang, A. Rykov, O.Y. Gutiérrez, Y. Zhao, S. Wang, X. Ma, J.A. Lercher, The synergistic effect between Ni sites and Ni-Fe alloy sites on hydrodeoxygenation of lignin-derived phenols, *Appl. Catal. B: Environ.* 253 (2019) 348–358, <https://doi.org/10.1016/j.apcatb.2019.04.065>.
- [27] C. Ciotonea, B. Dragoi, A. Ungureanu, C. Catrinescu, S. Petit, H. Alamdari, E. Marceau, E. Dumitriu, S. Royer, Improved dispersion of transition metals in mesoporous materials through a polymer-assisted melt infiltration method, *Catal. Sci. Technol.* 7 (2017) 5448–5456, <https://doi.org/10.1039/C7CY00963A>.
- [28] C.A. Teles, C. Ciotonea, A. Le Valant, C. Canaff, J. Dhainaut, J.-M. Clacens, F. Bellot Noronha, F. Richard, S. Royer, Optimization of catalyst activity and stability in the m-cresol hydrodeoxygenation through Ni particle size control, *Appl. Catal. B: Environ.* 338 (2023) 123030, <https://doi.org/10.1016/j.apcatb.2023.123030>.
- [29] A. Ungureanu, B. Dragoi, V. Hulea, T. Cacciaguerra, D. Meloni, V. Solinas, E. Dumitriu, Effect of aluminium incorporation by the “pH-adjusting” method on the structural, acidic and catalytic properties of mesoporous SBA-15, *Microporous Mesoporous Mater.* 163 (2012) 51–64, <https://doi.org/10.1016/j.micromeso.2012.05.007>.
- [30] J. Wang, Q. Liu, A simple method to directly synthesize Al-SBA-15 mesoporous materials with different Al contents, *Solid State Commun.* 148 (2008) 529–533, <https://doi.org/10.1016/j.ssc.2008.09.052>.
- [31] S. Chen, C. Ciotonea, A. Ungureanu, E. Dumitriu, C. Catrinescu, R. Wojcieszak, F. Dumeignil, S. Royer, Preparation of nickel (oxide) nanoparticles confined in the secondary pore network of mesoporous scaffolds using melt infiltration, *Catal. Today* 334 (2019) 48–58, <https://doi.org/10.1016/j.cattod.2019.01.064>.
- [32] Y. Wang, J. Yu, Y. Wang, Z. Chen, L. Dong, R. Cai, M. Hong, X. Long, S. Yang, In situ templating synthesis of mesoporous Ni-Fe electrocatalyst for oxygen evolution reaction, 23321–2330, *RSC Adv.* 20 (2020), <https://doi.org/10.1039/D0RA03111A>.
- [33] Y. Kathiraser, J. Ashok, S. Kawi, *Catal. Sci. Technol.* 6 (2016) 4327–4336, <https://doi.org/10.1039/C5CY01910A>.
- [34] P.M. de Souza, R.C. Rabelo-Neto, L.E.P. Borges, G. Jacobs, B.H. Davis, T. Sooknoi, D.E. Resasco, F.B. Noronha, Role of Keto intermediates in the hydrodeoxygenation of phenol over Pd on oxophilic supports, *ACS Catal.* 5 (2015) 1318–1329, <https://doi.org/10.1021/cs501853t>.
- [35] M.B. Griffin, G.A. Ferguson, D.A. Ruddy, M.J. Biddy, G.T. Beckham, J.A. Schaidle, Role of the support and reaction conditions on the vapor-phase deoxygenation of m-Cresol over Pt/C and Pt/TiO₂ Catalysts, *ACS Catal.* 6 (2016) 2715–2727, <https://doi.org/10.1021/acscatal.5b02868>.
- [36] C.A. Teles, P.M. de Souza, R.C. Rabelo-Neto, A. Teran, G. Jacobs, D.E. Resasco, F.B. Noronha, Hydrodeoxygenation of lignin-derived compound mixtures on Pd-Supported on various oxides, *ACS Sustain. Chem. Eng.* 9 (2021) 12870–12884, <https://doi.org/10.1021/acsschemeng.1c03720>.
- [37] X. Zhu, L. Nie, L.L. Lobban, R.G. Mallinson, D.E. Resasco, Efficient conversion of m-cresol to aromatics on a bifunctional Pt/HBeta Catalyst, *Energy Fuels* 28 (2014) 4104–4111, <https://doi.org/10.1021/ef500768r>.
- [38] C.A. Teles, C. Ciotonea, Nicolas Gomes, V.O.O. Gonçalves, A. Ungureanu, C. Catrinescu, M. Marinova, J.-M. Clacens, S. Royer, F.B. Noronha, F. Richard, Hydrodeoxygenation of m-cresol over Pd/Al-SBA-15 catalysts: effect of Al content on the deoxygenation reaction pathways, *Appl. Catal. A: Gen.* 641 (2022) 118686, <https://doi.org/10.1016/j.apcata.2022.118686>.
- [39] L. Nie, D.E. Resasco, Kinetics and mechanism of m-cresol hydrodeoxygenation on a Pt/SiO₂ catalyst, *J. Catal.* 317 (2014) 22–29, <https://doi.org/10.1016/j.jcat.2014.05.024>.
- [40] Y. Hong, H. Zhang, J. Sun, K.M. Ayman, A.J.R. Hensley, M. Gu, M.H. Engelhard, J.-S. McEwen, Y. Wang, Synergistic catalysis between Pd and Fe in gas phase hydrodeoxygenation of m-Cresol, *ACS Catal.* 4 (2014) 3335–3345, <https://doi.org/10.1021/cs500578g>.
- [41] H.-Y.T. Chen, G. Pacchioni, Role of oxide reducibility in the deoxygenation of phenol on ruthenium clusters supported on the anatase titania (1 0 1) surface, *ChemCatChem* 8 (2016) 2492–2499, <https://doi.org/10.1002/cctc.201600457>.
- [42] A.J. Foster, P.T.M. Do, R.F. Lobo, The synergy of the support acid function and the metal function in the catalytic hydrodeoxygenation of m-Cresol, *Top. Catal.* 55 (2012) 118–128, <https://doi.org/10.1007/s11244-012-9781-7>.
- [43] P.T.M. Do, A.J. Foster, J. Chen, R.F. Lobo, Bimetallic effects in the hydrodeoxygenation of meta-cresol on γ -Al₂O₃ supported Pt-Ni and Pt-Co catalysts, *Green. Chem.* 14 (2012) 1388, <https://doi.org/10.1039/C2GC16544A>.
- [44] M.S. Zanuttini, B.O. Dalla Costa, C.A. Querini, M.A. Peralta, Hydrodeoxygenation of m-cresol with Pt supported over mild acid materials, *Appl. Catal. A: Gen.* 482 (2014) 352–361, <https://doi.org/10.1016/j.apcata.2014.06.015>.
- [45] P.M. de Souza, L. Nie, L.E.P. Borges, F.B. Noronha, D.E. Resasco, Role of oxophilic supports in the selective hydrodeoxygenation of m-Cresol on Pd Catalysts, *Catal. Lett.* 144 (2014) 2005–2011, <https://doi.org/10.1007/s10562-014-1337-y>.

- [46] F. Yang, D. Liu, Y. Zhao, H. Wang, J. Han, Q. Ge, X. Zhu, Size dependence of vapor phase hydrodeoxygenation of m-Cresol on Ni/SiO₂ catalysts, *ACS Catal.* 8 (2018) 1672–1682, <https://doi.org/10.1021/acscatal.7b04097>.
- [47] P.M. Mortensen, J.-D. Grunwaldt, P.A. Jensen, A.D. Jensen, Influence on nickel particle size on the hydrodeoxygenation of phenol over Ni/SiO₂, *Catal. Today* 259 (2016) 277–284, <https://doi.org/10.1016/j.cattod.2015.08.022>.
- [48] X. Liu, W. An, C.H. Turner, D.E. Resasco, Hydrodeoxygenation of m-cresol over bimetallic NiFe alloys: kinetics and thermodynamics insight into reaction mechanism, *J. Catal.* 359 (2018) 272–286, <https://doi.org/10.1016/j.jcat.2018.01.006>.
- [49] H. Shafaghat, P.S. Rezaei, W.M.A.W. Daud, Catalytic hydrodeoxygenation of simulated phenolic bio-oil to cycloalkanes and aromatic hydrocarbons over bifunctional metal/acid catalysts of Ni/HBeta, Fe/HBeta and NiFe/HBeta, *J. Ind. Eng. Chem.* 35 (2016) 268–276, <https://doi.org/10.1016/j.jiec.2016.01.001>.